Interaction of dipolarization fronts within multiple bursty bulk flows in global MHD simulations of a substorm on 27 February 2009

Y. S. Ge,[1] J. Raeder,[1] V. Angelopoulos,[2] M. L. Gilson,[1] and A. Runov[2]

[1]   We performed a global MHD simulation of a well-studied substorm on 27 February 2009 (Runov et al., 2009) to understand the generation and large-scale evolution of dipolarization fronts within bursty bulk flows (BBFs). Conjugate, well-positioned Time History of Events and Macroscale Interactions During Substorms (THEMIS) observations from space and ground observatories provide significant constraints to the simulation model. The main substorm onset auroral brightening, at 0749 UT, was in the field of view of Fort Smith (FSMI), just poleward of a preexisting auroral arc. Two minutes later, the space probes recorded a sharp dipolarization front moving sunward, passing by THEMIS and traversing ~10 R_E along the magnetotail. Our global MHD model, OpenGGCM, driven by real-time solar wind/interplanetary magnetic field conditions, is able to reproduce the key features of these signatures. We show that the auroral breakup is caused by the strong flow shear and the flow vortices formed by the BBF flows. Rebound oscillations of the intruding BBF (consistent with recent observations by Panov et al. (2010a)) and filamentation of the front into 1 R_E size undulations are superimposed on the flow pattern. Further investigation of the interaction of the BBF and the dipolarization fronts (DFs) reveals that an observed bipolar Bz signature ahead of the DF is due to the interaction between two distinct plasmas emanating from multiple X lines: antisunward-moving flux tubes from a reconnection region at ~13 R_E and sunward-moving dipolarization region within a BBF from a midtail reconnection region at ~23 R_E.

1.   Introduction

[2]   During magnetospheric substorms, bursty bulk flows (BBFs) are often seen [*Baumjohann et al.*, 1990; *Angelopoulos et al.*, 1992, 1994]. BBFs in the plasma sheet have been considered one of the manifestations of near-Earth reconnection and are often found to be associated with substorm onsets [*Baumjohann et al.*, 1991, 1999]. Because of the association of BBFs and substorms, these fast flows have been studied in terms of substorm initiation [*Sergeev et al.*, 1995; *Shiokawa et al.*, 1998; *Nagai et al.*, 1998; *Miyashita et al.*, 2003]. As fast flows approach the inner magnetosphere, BBFs are decelerated by the dominant dipole magnetic field [*Hesse and Birn*, 1991; *Shiokawa et al.*, 1997]. The braking of fast earthward flows or the pressure gradient effects from the penetration of BBFs have been proposed by some authors to be able to produce the

current system, i.e., substorm current wedge, and thus trigger substorms [*Shiokawa et al.*, 1998; *Birn et al.*, 1999]. Other effects caused by the earthward BBFs, such as the plasma flow vortices, are also proposed to be the mechanism to drive the substorm current system [*Keiling et al.*, 2009]. Early localized computer simulations of tail dynamics also suggest that the buildup of the current wedge is closely connected to the slowdown and diversion of earthward flow and the shear at the edges of this flow [*Birn and Hesse*, 1991, 1996; *Scholer and Otto*, 1991]. However, the role of fast earthward flows in triggering substorms is still controversial, and some authors claim that the generation of a fast flow does not necessarily lead to a global substorm [*Lyons et al.*, 1999; *Ieda et al.*, 2001; *Ohtani et al.*, 2002a, 2002b]. On the other hand, it is believed that fast flows play an important role in the plasma sheet convection on the transport of plasma through the magnetosphere [*Birn et al.*, 2004]. Thus investigations of BBFs are important for better understanding the relation of near-Earth reconnection with substorm onsets and the coupling between magnetotail and ionospheric dynamics.

[3]   During BBF events, localized dipolarizations—increases of magnetic field elevation angle—are often

---

[1]Space Science Center, University of New Hampshire, Durham, New Hampshire, USA.
[2]Institute of Geophysics and Planetary Physics, University of California, Los Angeles, California, USA.
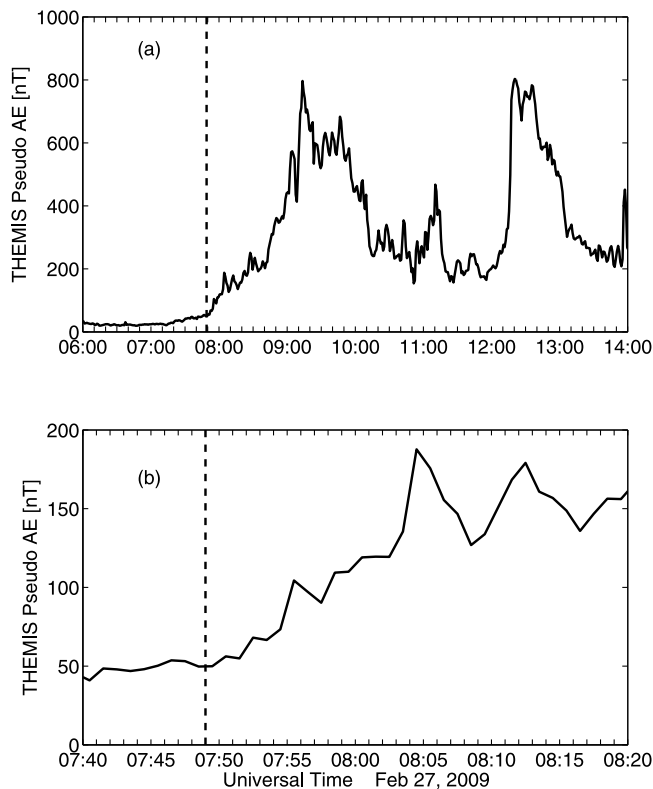
Figure 1. Thermal Emission Imaging System (THEMIS) pseudo-AE index is derived from the ground magnetometer data of THEMIS ground-based observatories (GBOs). The vertical dashed line marks the onset time for the AE index (0749 UT).

observed, which rapidly transport magnetic flux toward the Earth [*Nakamura et al.*, 2005, 2009]. This type of dipolarizations, which are also called transient dipolarizations, differ from the dipolarizations that are usually observed in the near-Earth plasma sheet at X ~10 R_E. The dipolarizations in the near-Earth plasma sheet are often interpreted as the magnetic field pileup effect when the fast flows are decelerated in the near-Earth tail region [*Hesse and Birn*, 1991; *Shiokawa et al.*, 1997]. The transient dipolarizations are often observed from the midtail plasma sheet to the near-Earth region [*Ohtani et al.*, 2004]. Two interpretations have been proposed to explain this type of dipolarization, the BBF-type flux ropes [*Slavin et al.*, 2003] and the nightside flux transfer events (NFTEs) [*Sergeev et al.*, 1992]. For those dipolarization fronts (DFs) near the leading edges of the earthward flows, *Slavin et al.* [2003] suggested that the secondary magnetic islands in the closed line regions form the BBF-type flux rope between a closed field line reconnection and a dominating open field reconnection. They also proposed an idea to explain the asymmetric bipolar change of the Bz component of the magnetic field at the DFs, i.e., that the transient DFs are usually observed to have leading dips of the Bz component. Here we call them "DF precursors." Slavin et al. suggested that the southward magnetic flux dissipates during the "re-reconnection" with the northward dipole dominant field when the flux rope is pushed earthward by the strong earthward flows from the dominating X line. The second model called these transient

dipolarizations the NFTEs and interprets them in terms of the impulsive reconnection [*Sergeev et al.*, 1992]. To investigate these DFs, two-dimensional two-fluid simulations have been performed by *Ohtani et al.* [2004]. In their box simulations, multiple X lines develop from the fragmentation of a current sheet and a secondary magnetic island forms between the primary and secondary neutral lines. This result provides a rough agreement of simulation time series with the observations, while the bipolar change of the Bz component in their simulations is rather symmetric. An effort using two-dimensional particle in cell box simulations to study the dipolarization front has been made by *Sitnov et al.* [2009]. In this simulation, a similar structure can be produced by transient reconnections in the magnetotail before the steady reconnection is established. The asymmetric bipolar change of the Bz component is reproduced in the simulations. However, the simulation is limited by the box dimension, which is 40 ion inertial lengths, and the structure can only propagate in either direction for about 1–2 R_E in their simulations.

[4] Recently, Time History of Events and Macroscale Interactions During Substorms (THEMIS) spacecraft have provided many new observations of the Earth's magnetotail with a spatial coverage from 30 R_E to 10 R_E in the tail plasma sheet. One of interesting observations made by the radial alignment of THEMIS spacecraft is the earthward-propagating transient dipolarization front during a substorm on 27 February 2009 [*Runov et al.*, 2009]. In this event, a coherent structure of dipolarization front and accompanying BBFs were found to propagate over 10 R_E from P1 and P2 (THEMIS-B and THEMIS-C) probe to P3, and P4 (THEMIS-D and THEMIS-E) pair close to the substorm onset. Thus it is an excellent event for our simulations to study the magnetotail dynamics, especially on the formation and evolution of the BBFs and the transient dipolarizations, which can provide better understanding of these dynamics and structures within the global picture of this substorm. In this paper, with the real-time solar wind/interplanetary magnetic field (IMF) condition inputs we use the global MHD model, OpenGGCM, which is coupled with the thermosphere-ionosphere modules to simulate this substorm event. In section 2 of this paper, we give the description of our simulation model and settings for this event. In section 3, we first discuss the observations from THEMIS ground-based observatories (GBOs) to determine the location and time of substorm onset, and we then review the in situ observations of the tail BBFs and DFs. In section 4, we show the comparison of our simulation results with both in situ and ground-based observations. We then show the formation and evolution of the transient dipolarization and the BBFs associated with the substorm revealed in our simulation. The interaction of these intruding BBFs and DFs with the background plasma is also discussed in this section. The main conclusions are summarized in section 5.

2. Global MHD Model: OpenGGCM

[5] The OpenGGCM is a global coupled model of Earth's magnetosphere, ionosphere, and thermosphere [*Raeder et al.*, 2008]. The magnetosphere part solves the MHD equations as an initial boundary value problem. The MHD equations are only solved to within ~3 R_E of Earth. The
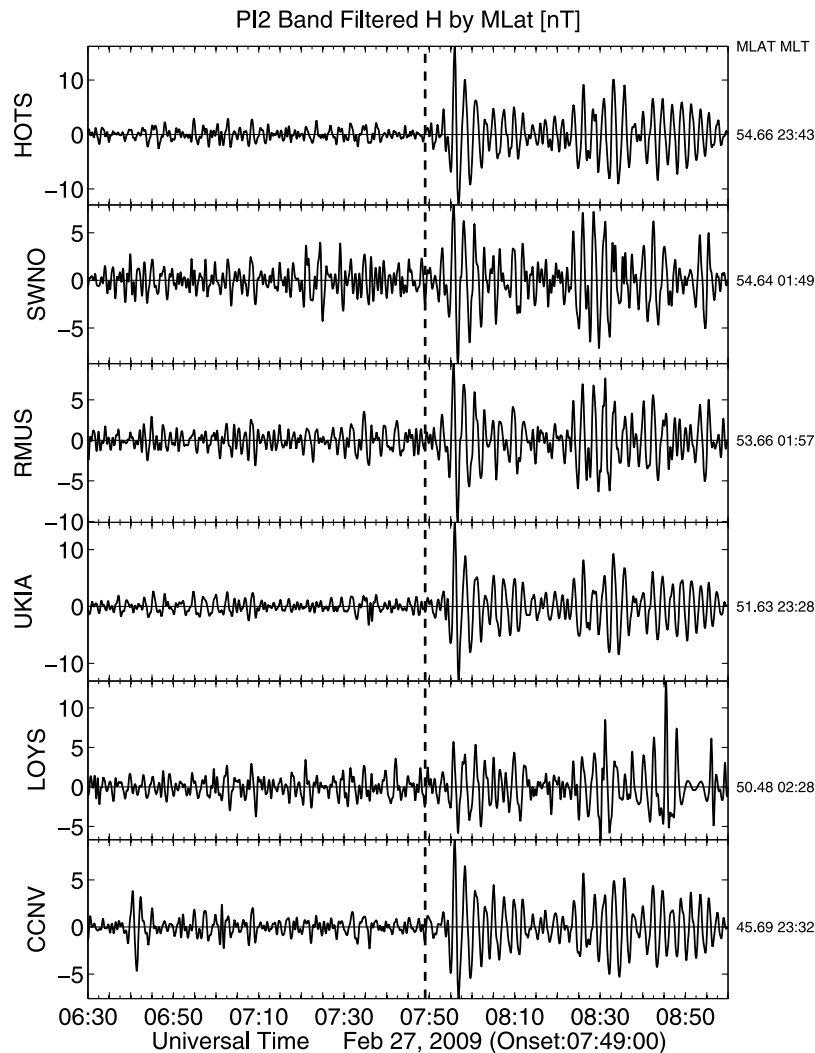
Figure 2. The H component of the midlatitude geomagnetic field is filtered within the frequency band of Pi2 pulsations. The vertical line marks the AE onset time. The midlatitude Pi2 onset appears a couple of minutes later than the AE onset.

region within 3 R_E is treated as a magnetosphere-ionosphere (MI) coupling region where physical processes that couple the magnetosphere to the ionosphere-thermosphere system are parameterized using simple models and relations. The ionosphere-thermosphere system is modeled using the NOAA Coupled Thermosphere Ionosphere Model (CTIM) [*Fuller-Rowell et al.*, 1996; *Raeder et al.*, 2001a, 2001b].

[6] In magnetosphere modules, OpenGGCM solves the resistive MHD equations on the nonuniform rectilinear grids, which have a minimum grid space at GSE $y = 0$ and $z = 0$ for the y and z directions, respectively, and at a point near the dayside magnetopause for the x direction. The solar wind and IMF conditions are the outer boundary conditions on the dayside, while those on the other five outer boundaries are free. The inner boundary conditions are derived from the ionospheric model.

[7] The coupling between the magnetosphere and the ionosphere is an essential part of the model because the ionosphere controls, to a large extent, magnetospheric convection by providing the resistive closure of the field-aligned currents (FACs) that are generated from the inter-

action of the solar wind with the magnetosphere [*Raeder et al.*, 1996, 1998]. Processes that occur in the near-Earth region on polar cap and auroral field lines and that are inherently kinetic have been parameterized in the model using empirical relationships. These processes include the field-aligned potential drops that are associated with upward FACs, electron precipitation caused by the field-aligned potential drops, and the diffuse electron precipitation that is caused by pitch angle scattering of plasma sheet electrons [*Kennel and Petschek*, 1966; *Lyons et al.*, 1979; *Robinson et al.*, 1987; *Weimer et al.*, 1987]. The electron precipitation parameters and the ionosphere potential are then passed to the CTIM ionosphere-thermosphere model, which is coupled to the MHD part of the code. CTIM [*Fuller-Rowell et al.*, 1996] is a three-dimensional dynamic model of the ionosphere and thermosphere with a long heritage, covering the globe from 80 km to several thousand kilometers of altitude, and following several neutral and ionic species and their photochemical interactions. CTIM computes self-consistently the ionospheric Pedersen and Hall conductances, which are then used to solve the ionospheric
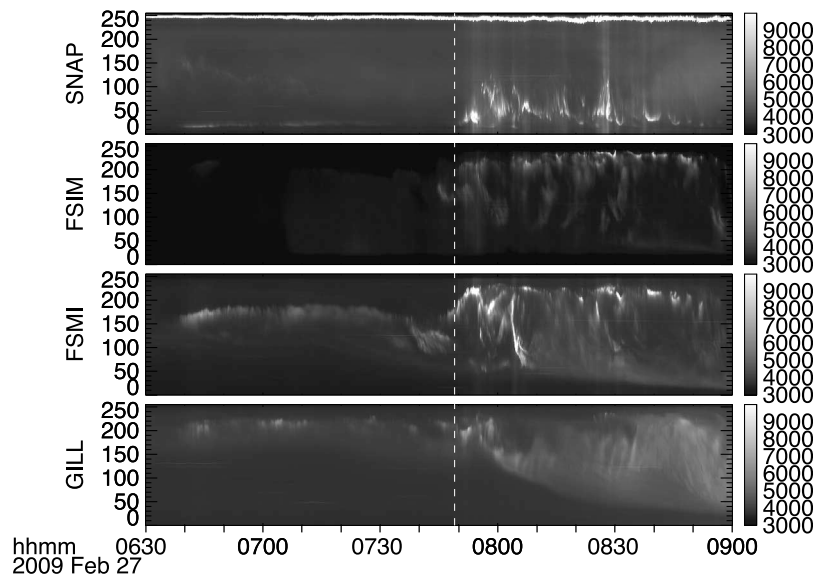
Figure 3. The keogram of ground all-sky-imager observations on stations SNAP (Snap Lake, [63.3°N, 249.1°E]), Fort Simpson (FSIM, [61.8°N, 238.8°E]), Fort Smith (FSMI, [60.0°N, 248.2°E]), and GILL (Gillam, [56.4°N, 265.3°E]). The vertical line is the AE onset time.

potential equation (see [*Raeder et al.*, 2001c], for details). A more detailed description of the latest version of OpenGGCM model can be found in *Raeder et al.* [2008].

[8] In this study, we simulate the THEMIS substorm on 27 February 2009 with the real-time solar wind and IMF conditions which have been propagated to our dayside boundary. The simulation domain has been set in the GSE $(-650, 24) \times (-48, 48) \times (-48, 48)$ R_E with about 37 million grid points. The distribution of grid in this simulation is similar to that in *Raeder et al.* [2008], and the minimum grid size is about 0.12 R_E near the Earth. The simulation starts from 0400 UT and ends at 1400 UT on 27 February 2009.

3. Overview of Observations on 27 February 2009 Substorm

3.1. Substorm Onset

[9] From the Pseudo-AE index derived from the magnetometer data of THEMIS ground-based observatories (GBOs) [*Mende et al.*, 2008; *Russell et al.*, 2008], two large substorms are identified on 27 February 2009. Figure 1a shows the Pseudo-AE index from 0400 to 1400 UT on 27 February 2009. A vertical dashed line at 0749 UT, preliminarily determined by the first sudden increase of the Pseudo-AE index, marks the AE onset time of the first substorm. Figure 1b zooms in the time around 0749 UT, and the faster increase of the AE index after 0749 UT is shown. Before 0749 UT, the auroral electrojet activity is small, i.e., AE is below 50 nT, while the following auroral electrojet activity is intense and both substorms have the maximum Pseudo-AE index above 800 nT. Although the AE index starts increasing faster after 0749 UT, the AE index reaches its first maximum almost 1 hour later, during which multiple intensifications of the auroral electrojet intensifications are present. In this study, we focus on the first substorm, since the second large substorm occurs at ~1155 UT, when the local midnight sector has passed the American continent

and, in addition, the THEMIS spacecraft are no longer radially aligned.

[10] The AE onset time is roughly consistent with the ground Pi2 pulsation onset in the midlatitude ground stations, which is another important indicator of substorm onset [*Hsu and McPherron*, 2007]. Figure 2 shows the filtered H-component (north-south component) of geomagnetic field within the frequency band of the Pi2 pulsations (2–25 mHz). A dashed line in Figure 2 marks the AE onset time, which is found to be a couple of minutes earlier than the midlatitude ground Pi2 onset. The Pi2 pulsations remain active after this onset, and multiple onsets are present afterward. However, even though the ground magnetic field data indicate a relatively quiet magnetosphere before the onset at 0749 UT, the all-sky imagers (ASIs) recorded an auroral pseudo-breakup 1 hour earlier. As shown on the keogram of ASI observations in Figure 3, a weak auroral brightening appears at the Fort Smith (FSMI) station at ~0640 UT, and it slightly intensifies and persists until the major onset at ~0749 UT that has strong intensifications and clear poleward expansion of auroral brightening region from FSMI to the further northern station SNAP (Snap Lake). The evolution of auroral activity at the major onset is shown by the full view of ASI observations on FSMI, GILL (Gillam), and SNKQ (Sanikiluaq) in Figure 4. The images of SNAP are not shown because of the overlap of field view with that of FSMI, and the stations west of FSMI are mostly covered by clouds. Figure 4a indicates a preexisting auroral arc extending from SNKQ to FSMI before the major breakup, which probably comes from the pseudo-breakup at 0640 UT. Another arc develops slightly poleward of the preexisting arc before ~0748 UT in the field of view of GILL and FSMI (Figure 4b). This new arc intensifies in the following 2 minutes (Figures 4c and 4d) and starts to expand at the west edge of field of view on GILL (Figure 4e). This constituted the main onset. From 0751 to 0754 UT as shown in Figures 4e–4h, the new arc fully expands poleward in the
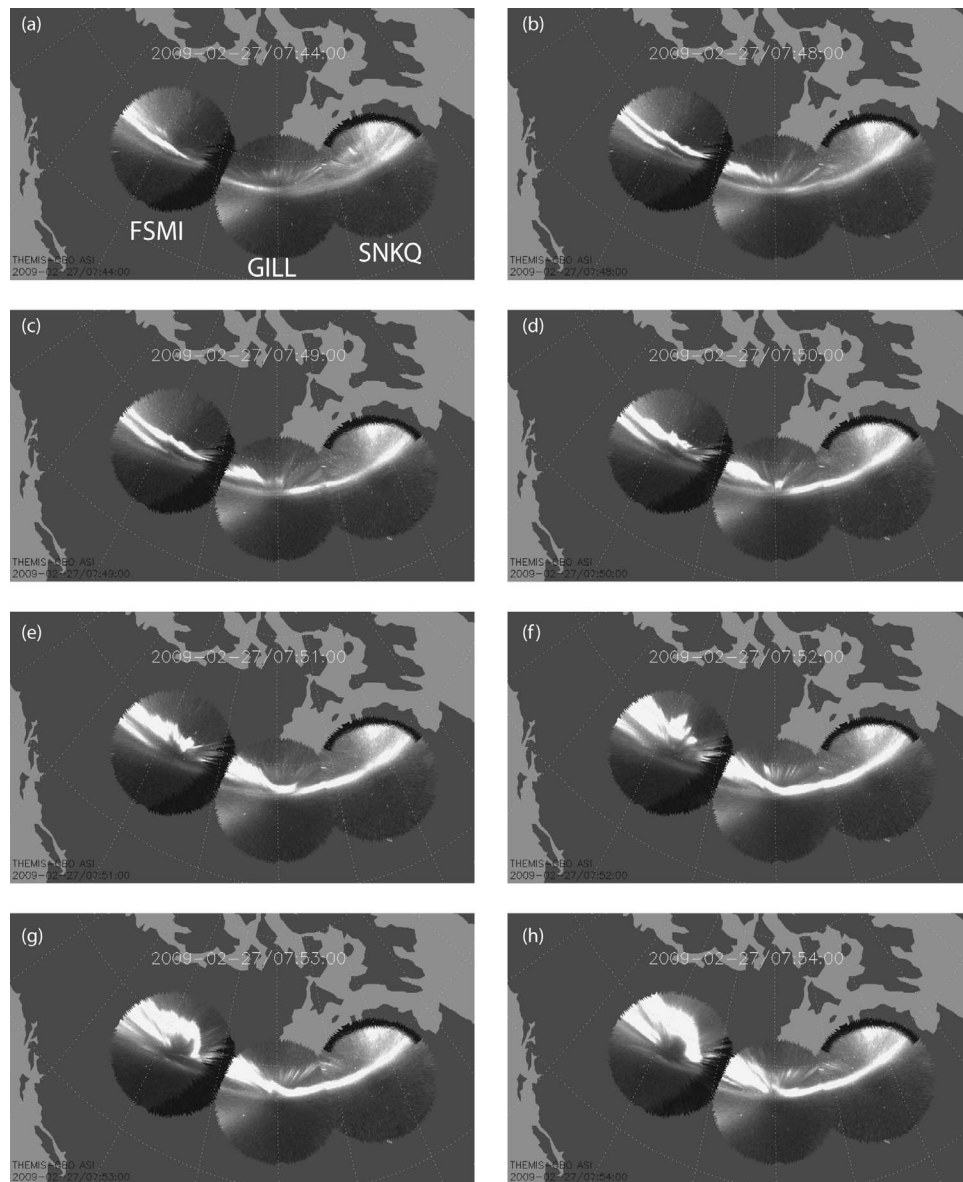
Figure 4. The full field of views of ground all-sky-imager observations on stations Fort Smith (FSMI, [60.0°N, 248.2°E]), GILL (Gillam, [56.4°N, 265.3°E]), and SNKQ (Sanikiluaq, [56.5°N, 280.8°E]) from left to right at eight times: (a) 0744 UT, (b) 0748 UT, (c) 0749 UT, (d) 0750 UT, (e) 0751 UT, (f) 0752 UT, (g) 0753 UT, and (h) 0754 UT.

field of view of FSMI. Meanwhile the preexisting arc dims at the local times of the poleward expanding arc, while the east part of preexisting arc (east of GILL) intensifies and appears to connect with the expanded aurora.

[11] Summarizing the ground-based observations for the substorm near 0749 UT on 27 February 2009, we find that the major onset of this strong substorm is preceded by an auroral pseudo-breakup, and this pseudo-breakup produced a long arc covering at least 5 hours in local time, which persists until the major expansion of auroral brightening at ~0751 UT. The major auroral expansion starts from a newly developed arc occupying the west part of GILL imager and the whole field of view of FSMI imager. The most significant poleward expansion starts at the location slightly poleward of the zenith of the FSMI imager.

3.2. Tail BBFs and Earthward Propagation of Dipolarization Front

[12] In the second tail season of THEMIS mission, from December 2008 to April 2009, the inclination angle of the orbits of midtail spacecraft (P1 and P2) were reduced so that the two spacecraft could better probe the thin current sheet of the magnetotail. On 27 February 2009, five THEMIS spacecraft were radially aligned and the propagation of tail fast flows and dipolarizations were well captured by THEMIS during the substorm onset near 0749 UT. Figure 5 shows the orbits of five THEMIS spacecraft in the Geocentric Solar Magnetospheric (GSM) coordinates from 0000 to 1200 UT on 27 February 2009. The outmost spacecraft P1 was located at ~21 R_E downtail near the local midnight
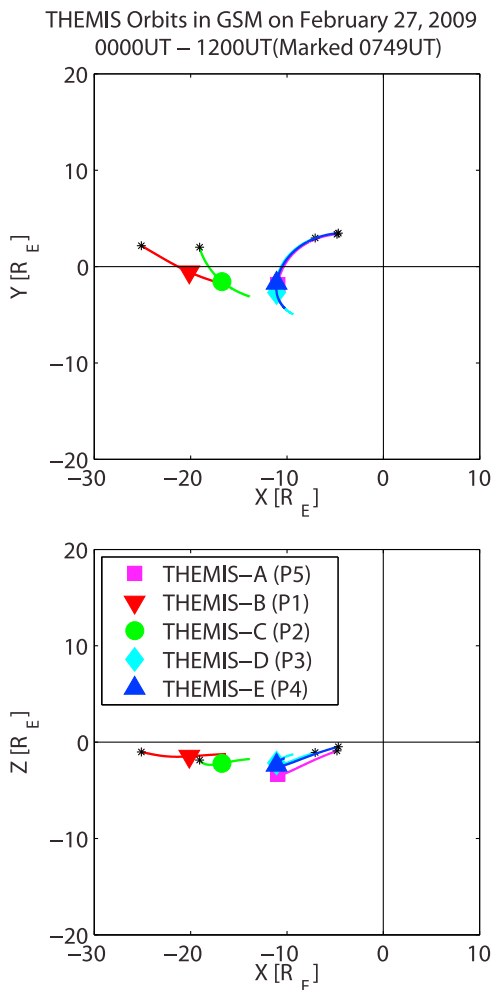
Figure 5. The projections of orbits of THEMIS spacecraft on the $x-y$ and $x-z$ planes in GSM coordinates on 27 February 2009. The spacecraft symbols mark the locations of the spacecraft at 0747 UT. The dark asterisk marks the starting point of THEMIS orbits.

sector, P2 at 17 R_E, and three inner spacecraft near 10 R_E downtail.

[13] Figure 6 shows the Bz component of the observed magnetic field and the x-component of the plasma velocity, both in GSM coordinates, at five spacecraft arranged from the top to bottom with P1 to P5 (THEMIS-A). The vertical dashed line marks the time of the Pseudo-AE onset (0749 UT). At 0751 UT, P1 observed a sharp dipolarization front, i.e., the sudden increase of the Bz component of magnetic field and decrease of the Bx component, following a transient decrease of the Bz component (i.e., the "DF precursor"). The structure has been referred to as the "dipolarization front" and has been shown to propagate earthward over 10 R_E to P3 and P4. Moreover, *Runov et al.* [2009] interpreted the observations as the leading edge of a plasma fast flow formed by a burst of magnetic reconnection in the midtail. Figure 6 shows that all dipolarization fronts (DFs) observed by five spacecraft are accompanied by the fast earthward flows, while the structures are a little different at different spacecraft. The DF precursor, i.e., negative Bz before the sharp DF, is most pronounced on P4 and less

significant on P1, while the Bz component remains positive on the other spacecraft even though it has a short dip before the DF. This difference was attributed to the limited size of BBFs and the curved shape of the horizontal cross-section of the plasma-depleted flux tube by *Runov et al.* [2009]. The propagation speed of the DF from 20 R_E to 11 R_E is estimated to be 300 km/s, both from propagation delay and from in situ velocity measurements. The front thickness is about 400–500 km [*Runov et al.*, 2009].

[14] In the following sections, we show that in our global MHD simulations, the main features of the 27 February 2009 substorm and the associated BBFs and DFs are reproduced. The results are then further analyzed to reveal the physical processes and to put the observations into a global context.

4.   Global View of Simulation Results of Substorm

[15] The solar wind and IMF conditions are used for the inputs of an OpenGGCM simulation. Figure 7 shows the time series of propagated solar wind/IMF conditions observed by WIND on 27 February 2009, which were obtained from the OMNIweb and have been propagated from the location of WIND (GSE [197, −25, −20]R_E) to the nose of the Earth's bow shock (GSE [11.92, −0.88, −0.49]R_E). The top of Figure 7 shows the magnetic field components processed using the MINVAR procedure [*Raeder et al.*, 2008], where BL is the maximum variance, BM is the intermediate variance, and BN is the minimum variance. The following three parts of Figure 7 show the three IMF components, where the red lines are the observations from WIND and the blue and green lines are results from, respectively, setting BN to zero and its average over the entire interval and transforming back to GSE. Since the input solar wind/IMF conditions have been propagated, the standard MINVAR procedure in OpenGGCM runs does not affect the input. The bottom two parts of Figure 7 show the solar wind plasma parameters, including the components of solar wind speed, solar wind temperature, number density, and plasma pressure, which are not affected by the MINVAR procedure. On 27 February 2009, the solar wind speed was on average of 500 km/s and the ion density was comparable to the average solar wind. Slightly before 0630 UT, the IMF Bz component gradually changed to southward and returned northward at ~0725 UT. The vertical dashed line marks the time of the AE onset for the substorm, and the IMF Bz component suddenly turns southward several minutes before the AE onset. The magnitude of the negative Bz is about 5–7 nT, and this southward IMF interval persists until 0945 UT. It appears that the sudden IMF southward turning may affect the following substorm onset. In our simulation results shown in the next section, we can find that a strong BBF is produced by the near-Earth reconnection after this IMF southward turning and that this BBF is responsible for the auroral breakup. However, in this case study, it is hard to test whether the southward turning of IMF is necessarily the trigger of this substorm onset, since the major tail reconnection could also be spontaneous. We cannot prove the causal effect of the sudden southward turning of IMF on the tail reconnection until we make a series of comparative simulations on the effects of IMF southward turning. In our simulations, spontaneous tail
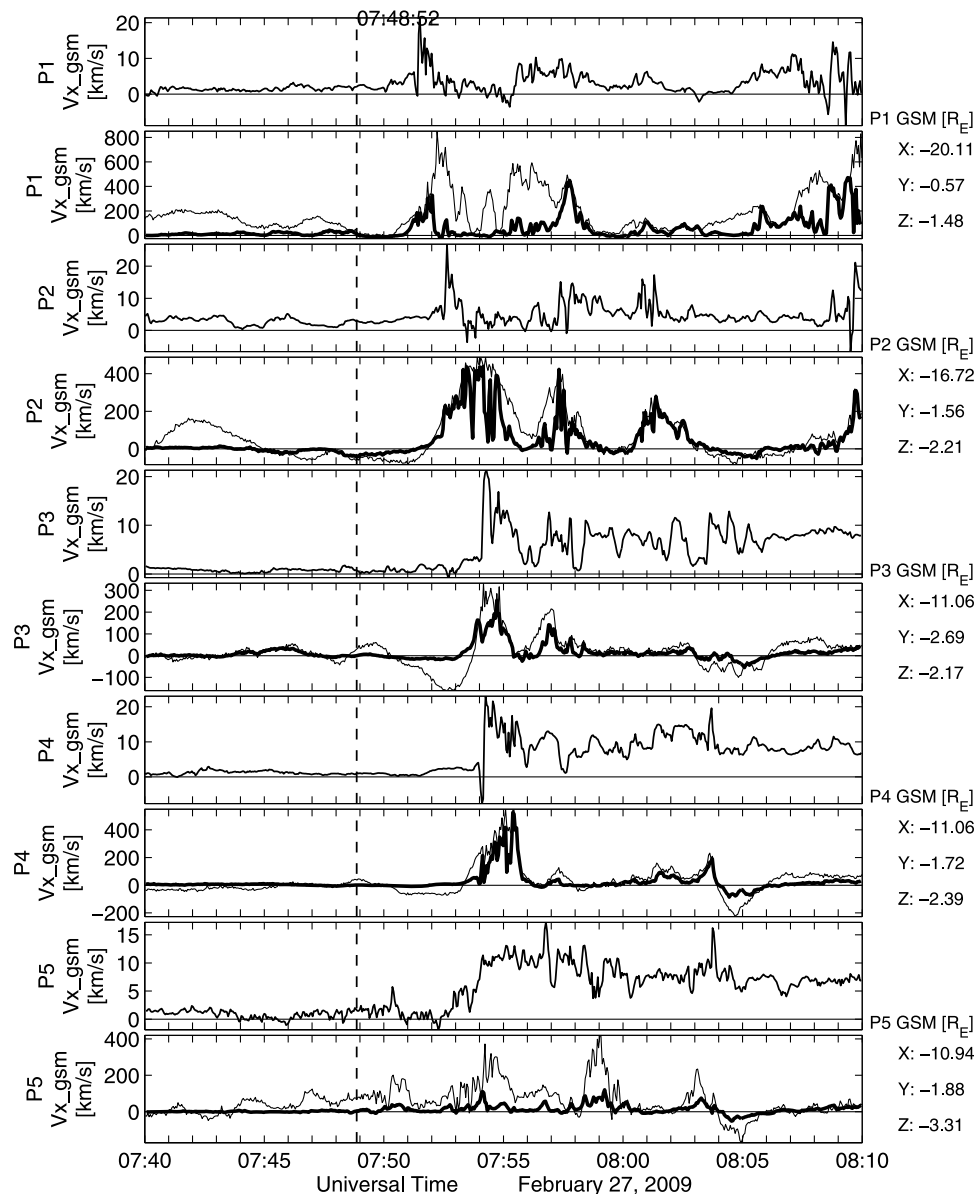
Figure 6. The Bz components and plasma velocity Vx components in GSM coordinates observed by five THEMIS spacecraft on 27 February 2009. The thin lines in the images showing plasma Vx components are the measurement of plasma velocity in GSM X direction by the THEMIS ESA instrument, while the thick lines in these images are the x-component of the perpendicular velocity to the local magnetic field orientation. The vertical line marks the AE onset time. The locations of five spacecraft at the AE onset time are provided at the right Figure 6.

reconnectionsdo happen when the magnetotail lobe is loading. In recent studies of this event, *Tang et al.* [2010] attributed this substorm onset to a tail lobe reconnection and suggested that the preceding pseudo-breakup may be related to transient reconnection on closed plasma sheet field lines. They suggested that this closed field line reconnection may precondition the current sheet for the following tail lobe reconnection.

4.1. Substorm Onset in OpenGGCM
4.1.1. Satellite Time Series
[16] The first comparison between our simulations and observations is performed on the time series taken in the

simulation at the same location of THEMIS spacecraft with the spacecraft measurements. Figures 8, 9, and 10 show the comparison of the magnetic field components, plasma flow components, and plasma number density at the virtual satellite VP1, VP2, and VP4 with the in situ observations. VP1, VP2, and VP4 annotate three virtual satellites which have positions in our simulation similar to those of P1, P2, and P4. To obtain better agreement between the time series of our simulation with observations, we slightly adjust the virtual satellite positions. For example, VP2 and VP4 are moved a little southward in our simulations. At 0749 UT, P2 and P4 are, respectively, located [−16.72, −2.08, −1.72] R_E and [−11.06, −2.29, −1.85] R_E in the GSE coordinates,
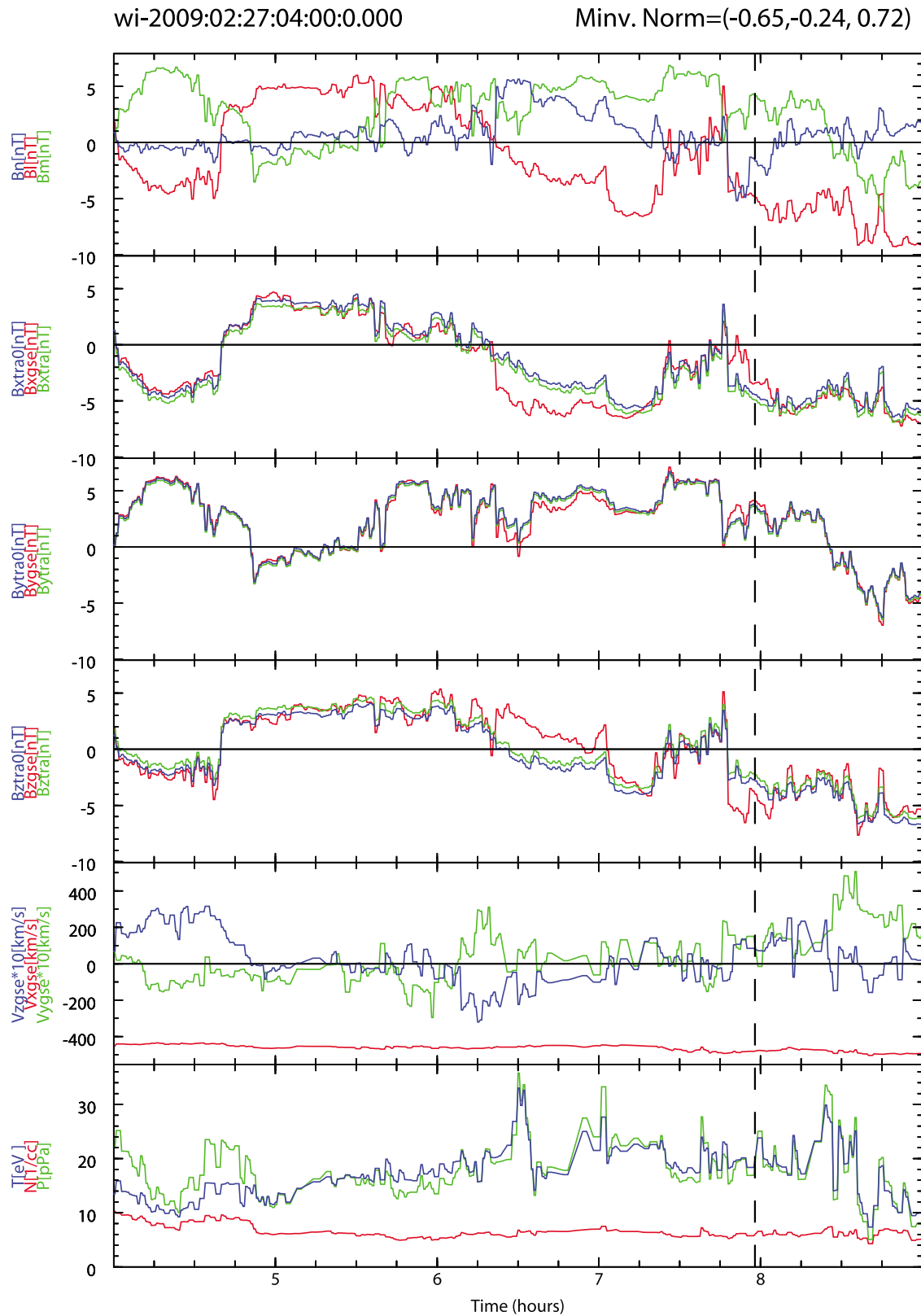
Figure 7. The solar wind/IMF conditions are processed by the MINVAR procedure and used as the input of the simulation on 27 February 2009 substorm. The detailed description of each part of Figure 7 can be found in the text. The two vertical lines mark the first IMF southward turning and the AE onset time, respectively.
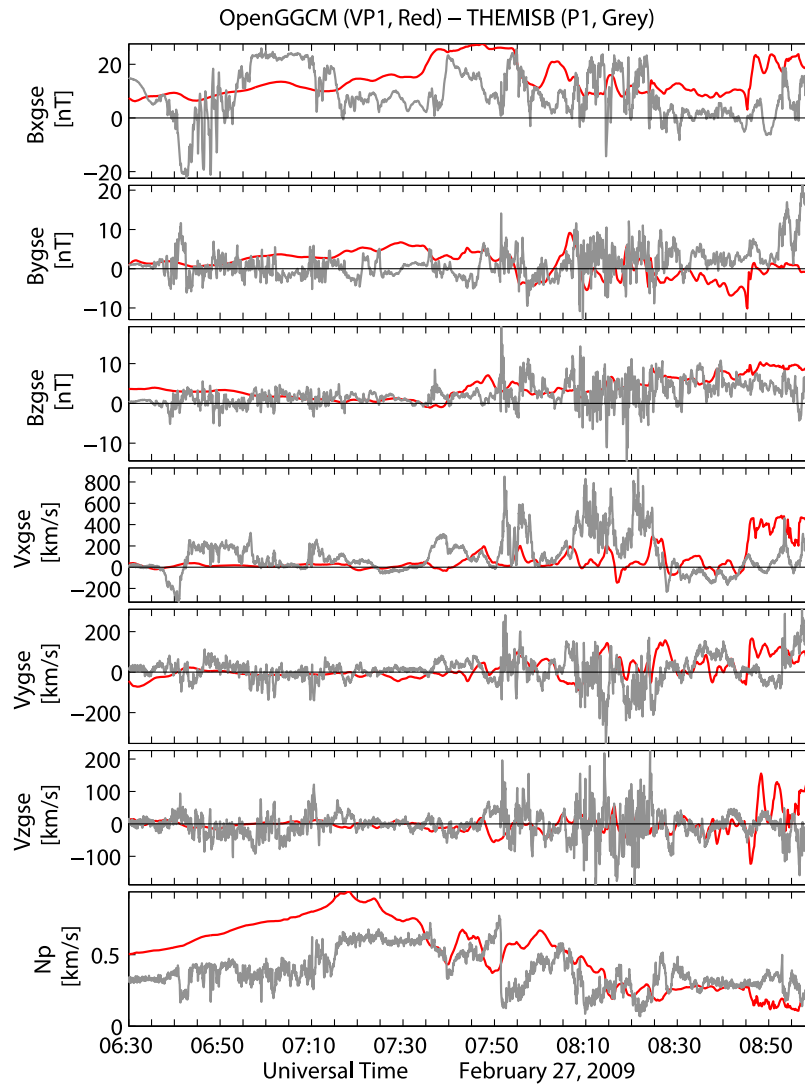
Figure 8. Comparison of the MHD state variables measured by P1 (black lines) and from the OpenGGCM simulations VP1 (red lines). The parts of Figure 8 show, from top to bottom, the three components of the magnetic field, the three components of plasma velocity, and the plasma number density.

while VP2 and VP4 are 1.0 R_E and 1.6 R_E below P2 and P4, respectively. The comparisons on P3 and P5 are omitted owing to their close positions with, and the similarity of their signatures to, those at P4. The dipolarizations of the magnetic field and the fast earthward flows are observed near the onset time on all three spacecraft. However, the features of dipolarizations are different at these three virtual satellites. On VP1, the dipolarization of the magnetic field is prior to the P1 observed DF and the increasing of the Bz component of the magnetic field is rather slow compared with the observations. In the simulation, the magnetic field gradually becomes more vertical, accompanied by the earthward fast flows as early as 0740 UT, and the fast flows are slower than those observed. The virtual satellite VP2 observed more similar dipolarizations and fast earthward flows with magnitude similar to the observations. At VP2, our simulations observe a much sharper dipolarization front than that at VP1, and the magnitude of the BBF reaches 500 km/s. The time difference between the DF in

simulations and that in observations is also much smaller on VP2. Furthermore, the following multiple dipolarizations at ~0845 UT and ~0916 UT are also observed in the simulation on VP2. The enhancement of the Bz component at the dipolarization front is short in duration, similar to the spike-shaped feature in the observation. The Bz component appears to decrease before the dipolarization but does not turn negative, similar to the actual observations shown in Figure 6. The plasma density in the simulation also generally agrees with the observations where a density enhancement appears before the DF and the density drops after the DF. This variation of the plasma density at the DF is consistent with the explanation of *Runov et al.* [2009] that the diamagnetic effect causes the plasma pressure and density to increase before the DF. The transient density enhancement before the DF is also present in the simulation during the interval of the Bz decrease. However, the DF formed in the simulation apparently has much larger
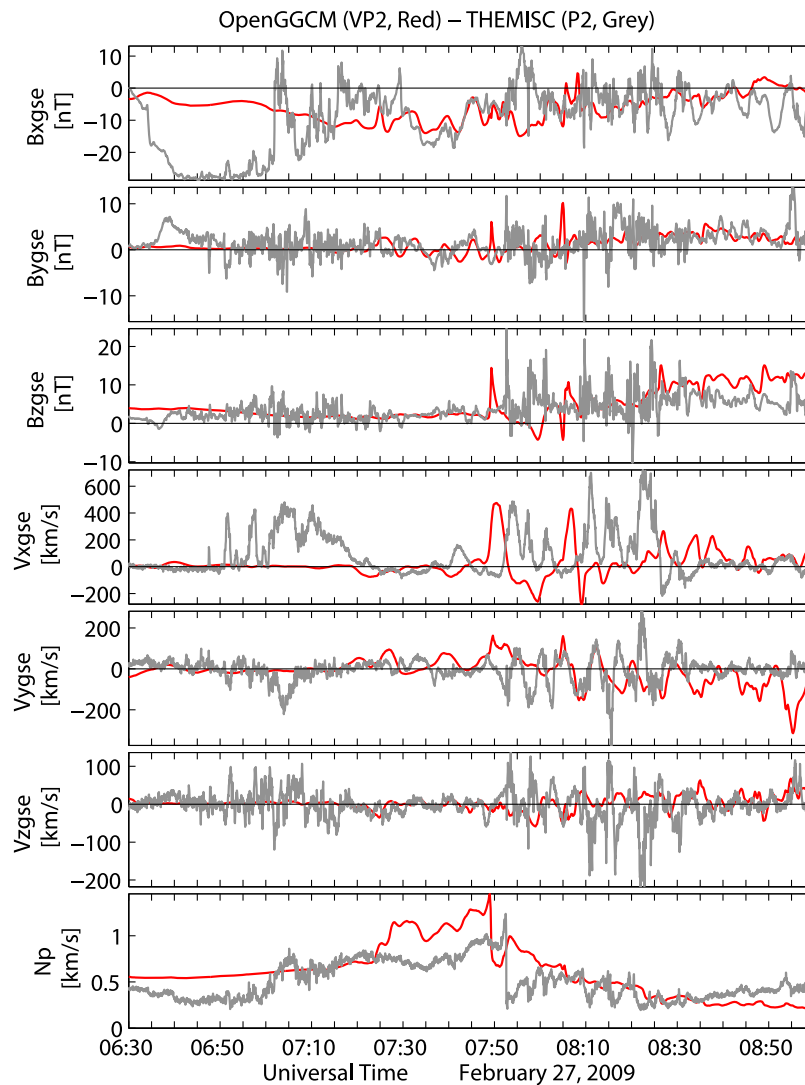
Figure 9. Comparison of the MHD state variables measured by P2 (black lines) and from the OpenGGCM simulations VP2 (red lines). The parts of Figure 9 show, from top to bottom, the three components of the magnetic field, the three components of plasma velocity, and the plasma number density.

thickness than that in observations, which is mainly due to the limited resolution of the MHD simulation.

[17] At the inner spacecraft such as VP4, the dipolarization is also present and a decrease on the Bz component appears before the sudden enhancement of Bz during the dipolarization. But the dipolarization front is not as sharp as that at VP2 and is accompanied by a slow earthward flow in our simulations (~150 km/s), which arrives at the virtual VP4 2 minutes later than that in the observations. Another strong dipolarization also appears 12 minutes later than the observed DF. The time delay of the first DF arrival between VP2 and VP4 is 2–3 minutes longer than that between P1 and P2. This difference is probably caused by the fact that the BBF slows down earlier in our simulation than in observations. The speed of fast flows at VP2 is comparable to that observed by P2, while VP4 observes a much lower earthward flow than P4. Despite the different time delay, we find that the DF signatures are also seen at VP4 after we move VP4 closer to the neutral sheet. A clear "dipolarization

precursor" (or the Bz dip) appears before the first dipolarization at VP4 (as shown in the third part of Figure 10), and an even greater Bz decrease is found before the second dipolarization 10 minutes later. In the following sections, we show that the second dipolarization at VP4 is in fact the near-Earth dipolarization which is caused by the pileup of magnetic flux. We also note that the negative Bz component before the DF in observations has the largest magnitude at P4, which is shown in the following sections to be similar to the DF in the near-Earth region in the simulation and can be explained by the evolution of the DF structure during its propagation.

4.1.2. Aurora Breakup

[18] To investigate the auroral activity, the OpenGGCM produces the energy flux and the mean energy of two populations of precipitating electrons. The first population is the thermal electron flux from the inner magnetosphere, which is unstructured and representative of the diffuse aurora. The second population is made up of electrons that
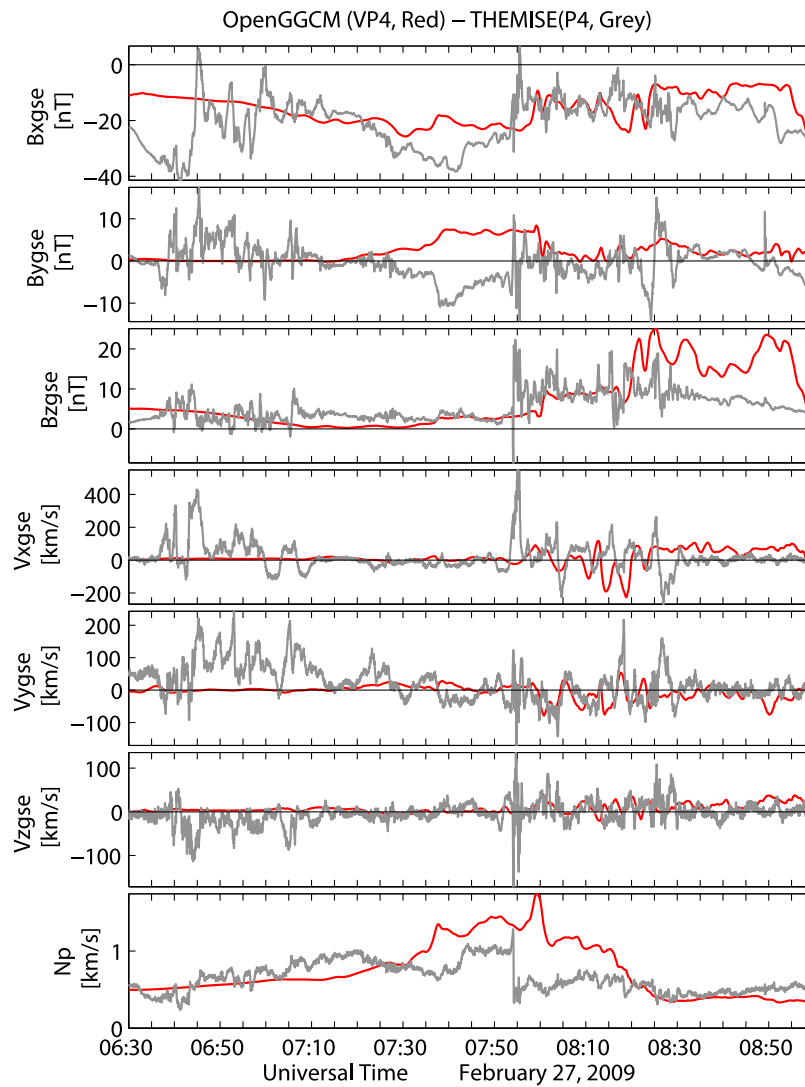
Figure 10. Comparison of the MHD state variables measured by P4 (black lines) and from the OpenGGCM simulations VP4 (red lines). The parts of Figure 10 show, from top to bottom, the three components of the magnetic field, the three components of plasma velocity, and the plasma number density.

have been accelerated in regions of upward FAC, which is highly structured and representative of the discrete aurora. In Figure 11, we show a polar view of the northern hemisphere at six times. The energy flux of precipitating electrons that are produced by FACs is color coded in units of milliwatts per square meter, and the thick black line shows the polar cap boundary (PCB).

[19] The first part of Figure 11 shows the aurora and PCB at 0631 UT, when the solar wind is weakly southward. The PCB is located above 75° at most local times and it extends to lower latitudes at the midnight sector. The auroral activity is fairly week. At 0748 UT, the IMF has turned southward. The PCB clearly expands toward lower latitudes in all local times, and in the midnight sector the PCB reaches 70°, which indicates that the magnetic energy is being convected into and stored in the tail lobes during the growth phase of the substorm. At the dawnside sectors, a long-extending arc appears which extends almost to FSMI, and a small intensification near FSMI (i.e., the blue dot shown in Figure 11)

starts to develop. This auroral brightening starts to expand and move westward at 0751 UT, when the ground-ASI observed the auroral poleward expansion on FSMI. Eventually the brightening region moves west of 2200 LT and merges with the preexisting aurora in the duskside sectors. In summary, the OpenGGCM closely reproduces the auroral breakup at the same time and location of the ground-ASI observations. However, since the observations west of FSMI are contaminated by clouds, we cannot compare the extent of the westward traveling of the simulated aurora with the observations. The causes of the westward motion of the simulated aurora are better revealed and further discussed in the following section.

4.2. BBFs and Dipolarization Fronts in OpenGGCM

4.2.1. Association of BBFs and Auroral Breakup

[20] To understand the physical processes that trigger this substorm onset, we investigate the relation of tail BBFs and dipolarizations with the substorm auroral breakup through
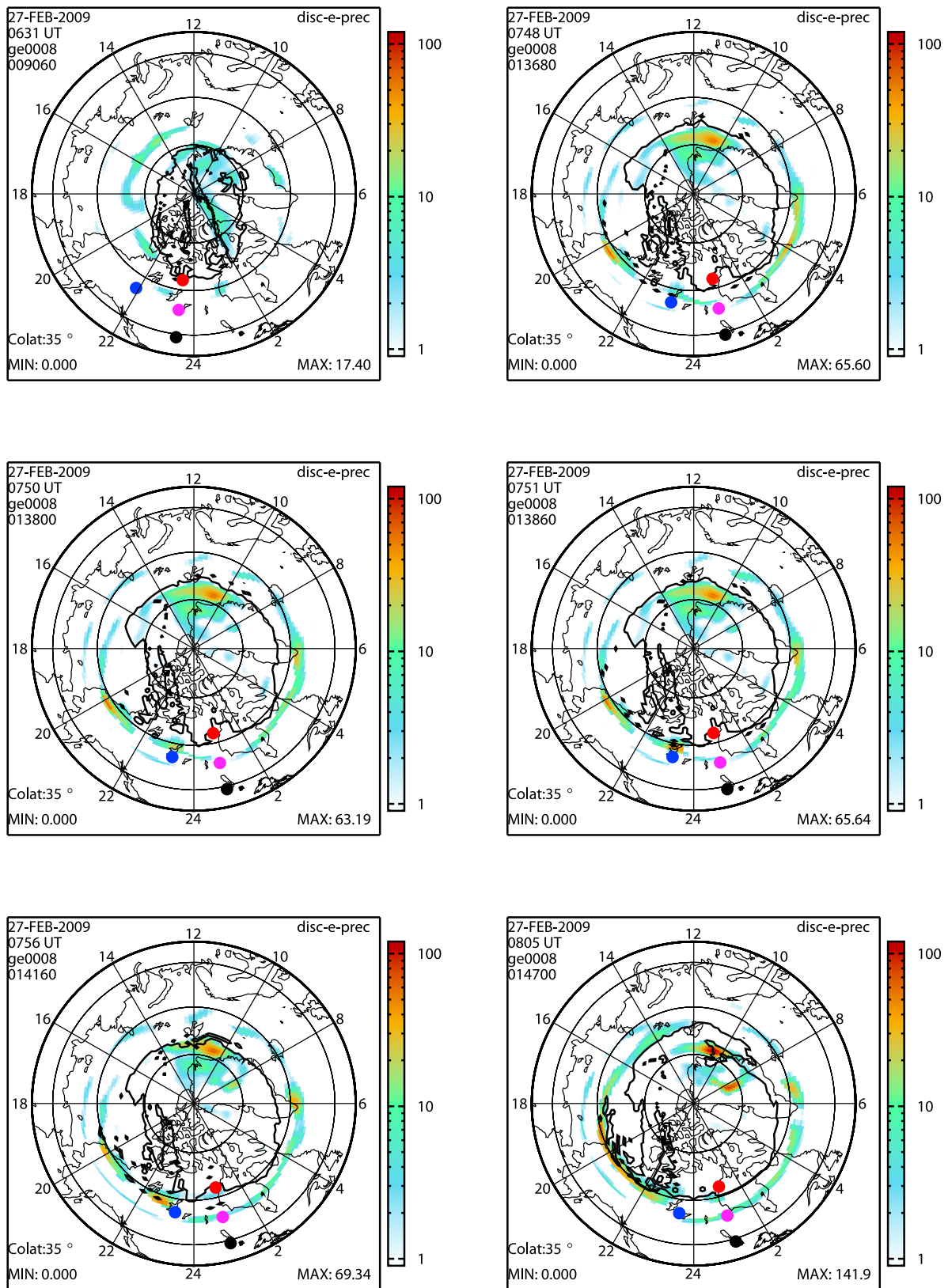
Figure 11. Polar view of the northern hemisphere. The color coding shows the energy flux of acceler-ated electrons, which serves as a proxy for auroral emissions. The thick black line is the polar cap bound-ary. The blue, magenta, red, and black dots mark the locations of the ground stations: FSMI, GILL, RANK, and PINA, respectively.
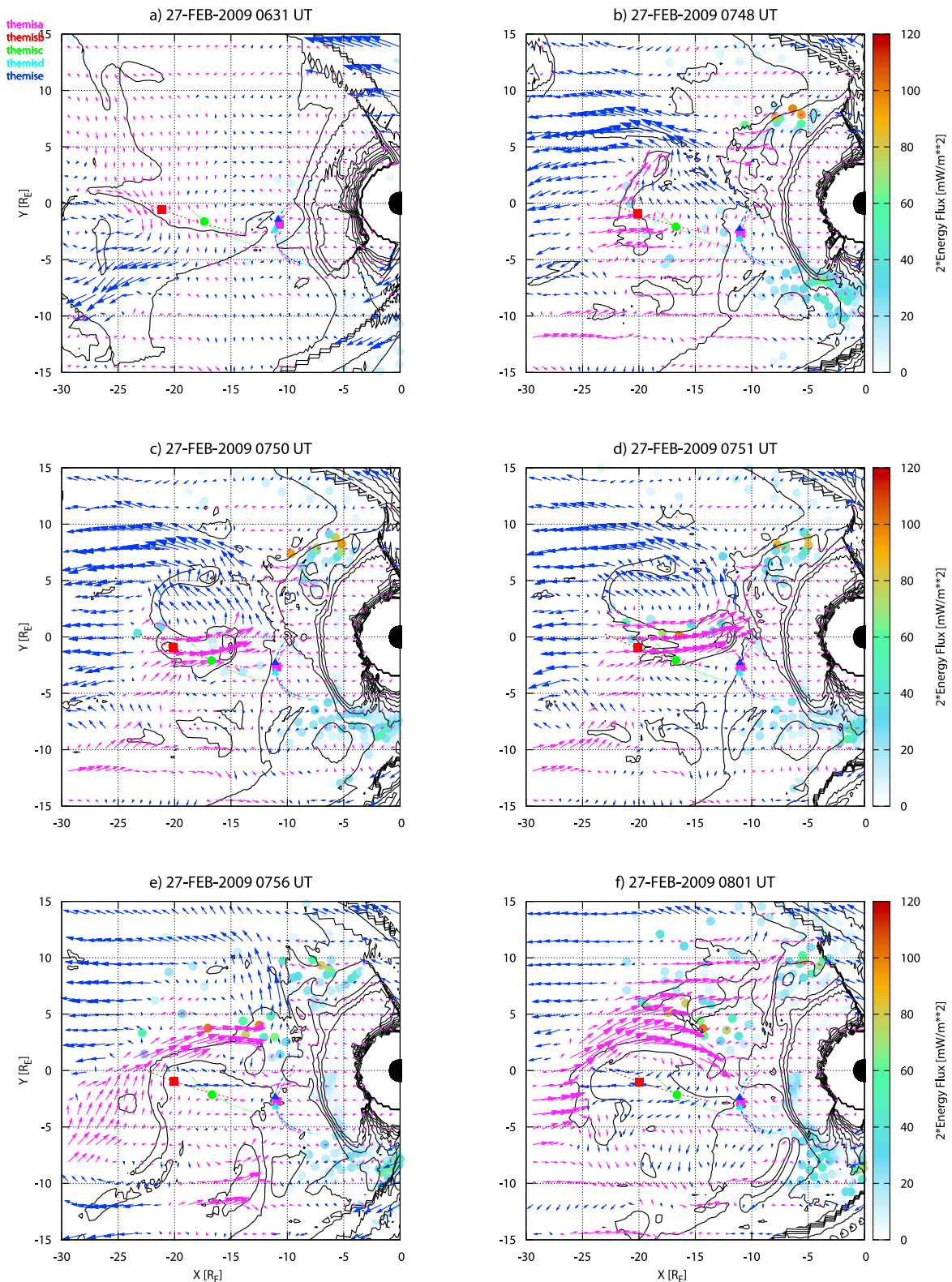
Figure 12. The projection of the flow vectors and mapped auroral emissions on the $x - y$ plane from the central plasma sheet plane, which is determined by the maximum beta value. The magenta and blue arrows show the flow vectors that are pointing earthward and tailward, respectively. The locations of five THEMIS spacecraft (or virtual satellites) and a part of their orbits on 27 February 2009 are shown in different colors: red, VP1; green, VP2; cyan, VP3; blue, VP4; and magenta, VP5. The black lines are the contour of the Bz component of the magnetic field. The color-coded solid circles are the mapped auroral emissions on this plane.

this global simulation. In Figure 12, a map of magnetospheric flows is made in the central plasma sheet plane that is determined in our simulations by the maximum of the β (the ratio of plasma pressure to magnetic pressure), i.e., at the center of the current sheet. The color of the flow vectors is determined by the x-component of plasma flows: blue for tailward flows and magenta for earthward flows. The discrete solid color-coded circles represent the locations where the auroral brightening regions map into the tail plasma sheet plane. The black lines in Figure 12 are the contours of the Bz component in this plane. The orbits of THEMIS spacecraft (or virtual satellites) are also shown in these plots: the red square represents VP1, the green circle represents VP2, the cyan triangle represents VP3, the blue triangle represents VP4, and the magenta diamond represents VP5.

[21] At 0631 UT (Figure 12a), the magnetotail is relatively quiet and tail flows are very small, although the IMF is weakly southward. At around 0734 UT, magnetic reconnection occurs at around X = −13 R_E and in the premidnight sector after the IMF turns northward at around 0728 UT, which is shown in Figure 12b at 0748 UT. Strong tailward flows are produced from this reconnection site while the earthward flows are initially slower because of the close location of the reconnection site to the inner magnetosphere. It is found later that the earthward flows gradually enhance, penetrate farther earthward, and are deflected toward dusk sectors. These diverted earthward flows produce the FAC to generate the discrete aurora at the premidnight sectors that is shown in Figure 11. In Figure 12c (0750 UT), this duskside aurora persists and becomes more pronounced. At the postmidnight or dawnside sectors, another moderate earthward flow appears to drive the FAC as the flow slows down and is diverted. This FAC is responsible for the weak auroral brightening in the dawnside sectors corresponding to the preexisting arc in Figure 11. However, the BBFs responsible for the auroral breakup on FSMI at the major substorm onset are generated from an X-line located at X = −23 R_E as shown in Figure 12c. This X-line extends from postmidnight sectors to the local midnight, with a width of about 6 R_E in the y-direction. The width of the BBF from this reconnection site is narrower, about 4 R_E. This earthward BBF travels from the reconnection site at X = −23 R_E to near X = −10 R_E, where the dipole field becomes dominating and slows it down. More importantly, it is found in Figure 12d that the auroral breakup region at 0751 UT maps into a broad region along the west side edge of the earthward BBF channel on the central plasma sheet plane. The FAC associated with this auroral breakup at 0751 UT is probably produced by the strong flow shearing at this region, which is further enhanced by the tailward flows west of the preexisting inner magnetic reconnection site. At this time, P1 and P2 are located close to the meridian of the BBF channel, while the VP3, VP4, and VP5 probes miss the BBF in our simulations. Also in our simulations, the plasma flow speed at VP1 is smaller than observations, which is probably due to the fact that VP1 is farther away from the central plasma sheet than in observations. But with a slight adjustment of the VP4 z-position, we successfully reproduce the DF signature on VP4. In our simulation, the neutral sheet is slightly lower than in the observations, which makes the original positions of P2 and P4 farther away from the central plasma sheet.

Our adjustments of the z-position of VP2 and VP4 not only results in better agreement of the Bx components but also enables us to reproduce the DF signatures. This result indicates that the width of the BBF channel or DF in the z-direction is also highly limited, which is also consistent with the analysis of *Runov et al.* [2009].

[22] Several minutes later, the X-line retreats tailward beyond 30 R_E and the flow channel appears to shift toward earlier local times. This westward motion of the flow channel is initiated by a small westward component of BBF when it comes out of the reconnection region. In Figure 12e, we find that a strong dipolarization region develops in the midnight sector, which further diverts the BBF westward. Along with the local time change of the BBF, the corresponding auroral breakup region moves westward. The westward traveling surge (WTS) has also been clearly demonstrated in the "first light" substorm of THEMIS and simulated by the OpenGGCM [*Raeder et al.*, 2008]. The speed of WTS was shown to agree on the ground and in space [*Angelopoulos*, 2008]. It is also worth noting that the region where the earthward BBF slows down or is diverted also moves tailward along with the pileup of the magnetic flux in the near-Earth tail and the BBF stops at around X = −15 R_E 10 minutes after the substorm onset (at 0801 UT; see Figure 12f).

4.2.2. Propagation and Evolution of Dipolarization Front

[23] To understand the relation of tail reconnections with the formation of the observed dipolarization front (DF), we zoom in on the regions where the BBF generated from the X-line is flowing and where the dipolarization region is evolving and propagating. In Figures 13 and 14, we show the vector field of tail flows and color contours of the Bz component in the near-Earth and middle tail region on the same central plasma sheet plane as that in Figure 12. The midtail reconnection produces multiple BBFs that pass through the near-Earth tail at different local times. The first BBFs from the midtail X-line travel earthward and also duskward, producing a region with the Bz enhancement in the front of the BBF. As we mentioned in the previous section, there is another reconnection site closer to the Earth, at around X = −13 R_E. The strong tailward flows accompanied by the southward magnetic flux from this reconnection site encounters the first BBF from the midtail X-line at 0747 UT (Figure 13a), which prevents the earthward BBF from its farther inward propagation and pushes it farther duskward. During this process, the dipolarization front is steepened. As shown in the next parts of Figure 13 and also in Figure 14, the first BBF from the midtail reconnection is eventually pushed back by the strong tailward flows from the inner reconnection and dissipates in the dusk flank. This dissipation process is similar to the "re-reconnection" concept in the multiple X-line scenario suggested by *Slavin et al.* [2003].

[24] Accompanied by the strong tailward flows, the Bz component is predominantly negative, which is typical for the Bz component on the tailward side of a reconnection site. However, this strong tailward flow from the inner magnetic reconnection is not able to or is not in the right local time to fully stop the second earthward BBF of the midtail reconnection from penetrating into the near-Earth region, and neither can the southward magnetic flux com-
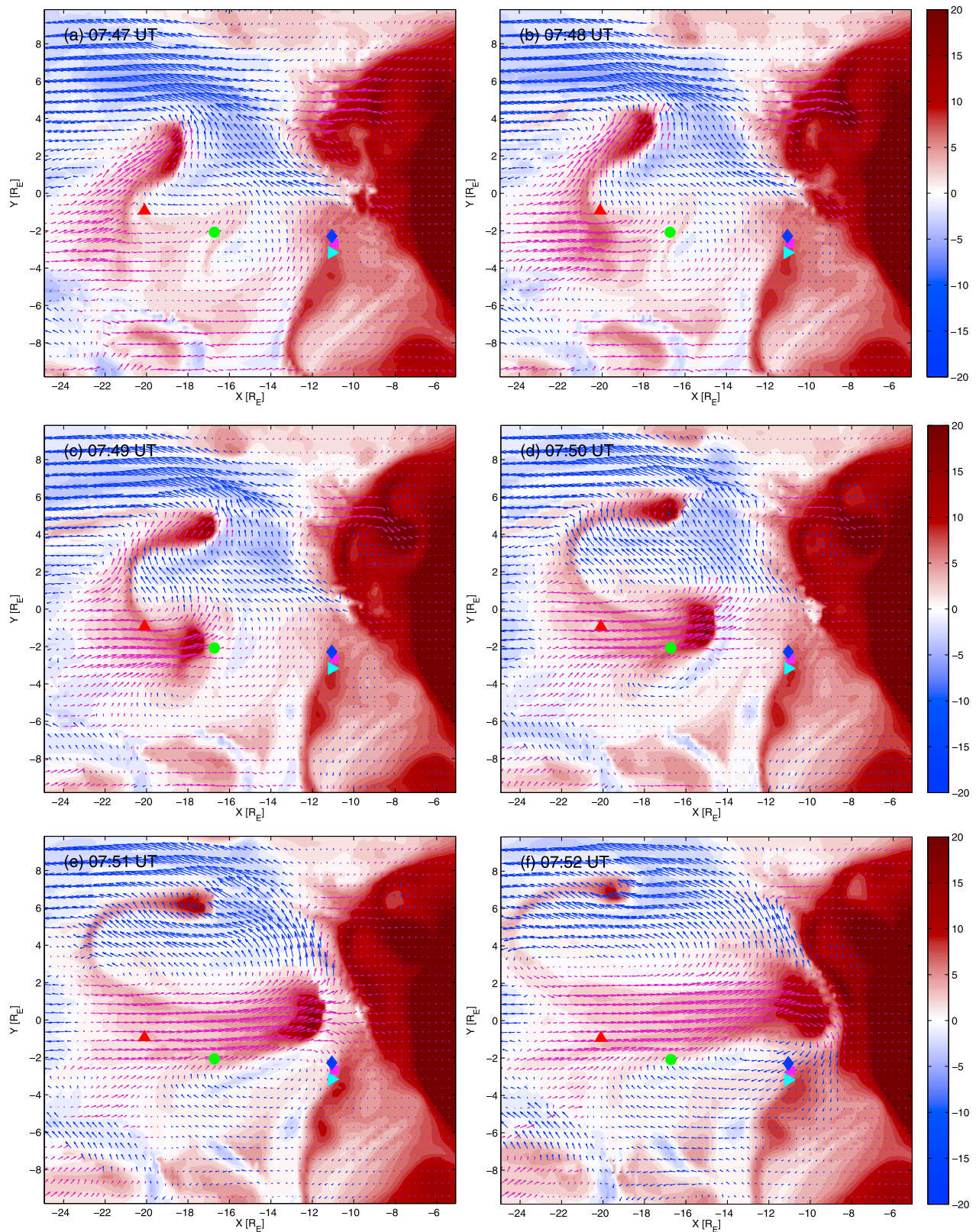
Figure 13. On the same plane as that shown in Figure 12, the flow vectors and color-coded contours of the Bz component of the magnetic field in the near-tail and midtail regions are shown at six times from 0747 UT to 0752 UT. The magenta and blue arrows show the flow vectors that are pointing earthward and tailward, respectively. The locations of five THEMIS spacecraft (or virtual satellites) are shown with the same color coding as that in Figure 12.
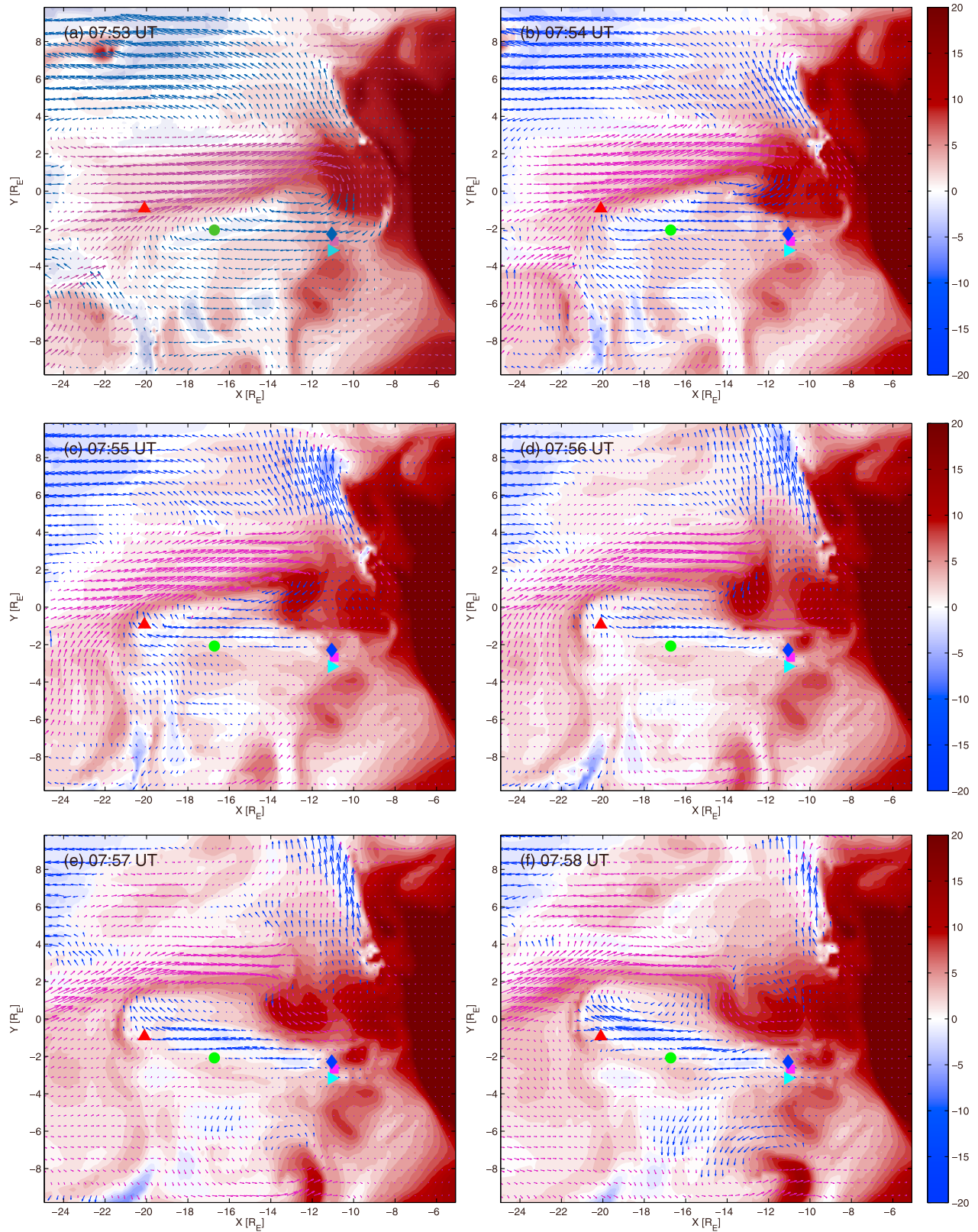
Figure 14. On the same plane as that in Figure 12, the flow vectors and color-coded contours of the Bz component of the magnetic field in the near-tail and midtail regions are shown at six times from 0753 UT to 0758 UT. The magenta and blue arrows show the flow vectors that are pointing earthward and tailward,
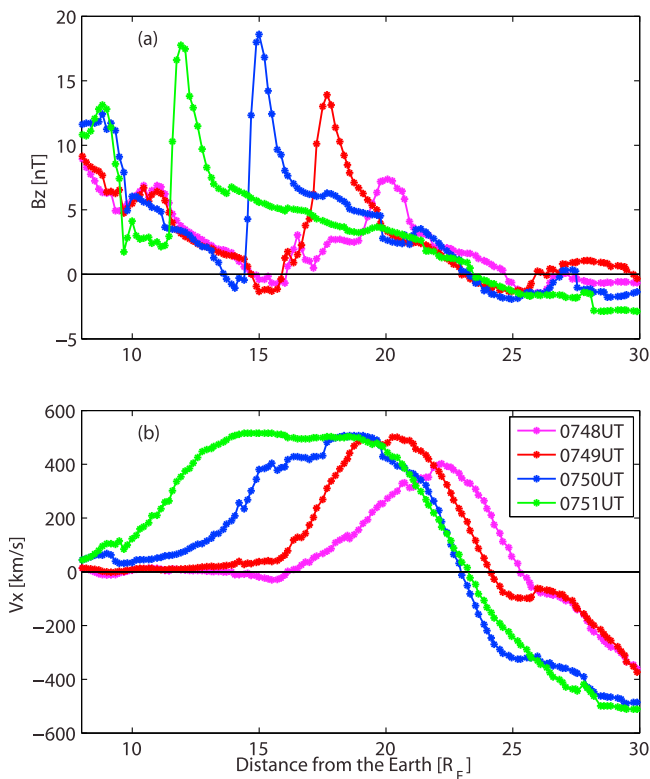
Figure 15. (a) Bz component and (b) Vx component profiles are taken along four radial lines in the plasma sheet plane at four times and at four different local times. The dots on the lines are the grid locations in the simulation.

pletely "re-reconnect" the intruding enhanced northward flux. The major BBF from the midtail reconnection line that is responsible for the auroral breakup still interacts with the tailward flows and southward magnetic flux from the inner reconnection. This BBF initially does not produce a very strong dipolarization region (see Figure 13a at 0747 UT). The first distinct dipolarization region from this BBF starts to form at 0748 UT (Figure 13b) at X = −20 R_E. In the front of this BBF, the dipolarization region begins to grow and, more importantly, the Bz component enhances. At 0749 UT (Figure 13c), this dipolarization region and BBF encounter the negative Bz region brought by the tailward flows from the inner reconnection. Along with the farther earthward penetration of this structure, the front of this dipolarization region becomes steeper and its southward Bz region becomes more distinct (see Figure 13d at 0750 UT). Meanwhile, the southward Bz region in front of this earthward traveling dipolarization front is also compressed and becomes narrower. During this process, a structure similar to the dipolarization front (DF) observed by THEMIS has formed by a distinct Bz enhancement region and a narrow region with negative Bz or smaller Bz component than the background. The scale size of this structure is limited in the y-direction to 2–3 R_E; it is propagating through the midtail region into the inner magnetosphere.

[25] To more clearly illustrate the formation and evolution of this DF structure in our simulation, we take four radial cuts at four times and at four XZ planes through the center of the BBF channel, which changes its local time during the

earthward propagation. Figure 15 shows the Bz components of the magnetic field and the Vx components of the plasma flow for these four cuts. The grid locations are also shown in the four lines by the dots. At a distance of 25 R_E to the Earth, the Bz component and the Vx component reverse their signs, showing the midtail reconnection. The inward-moving locations of four Bz peaks indicate the earthward propagation of the dipolarization front. It can be seen that there are regions of decreasing or negative B_z preceding the B_z peaks. The earthward fast flows arise ahead of the arrival of DF, which is consistent with THEMIS observations [*Runov et al.*, 2009]. As the structure travels closer to the Earth, the dipolarization peak becomes higher and the Bz decreasing region becomes narrower. However, the peak speed of BBF does not significantly change, but the length of this BBF channel appears to become longer. It is also found that along the earthward propagation of this structure, the thickness of DF becomes smaller, i.e., the DF becomes steeper while the profile of the Vx component does not significantly change during the propagation. The steepest DF has a thickness of only two or three grid cells across, suggesting that simulation becomes underresolved by the simulation grid size. It is also interesting that the last B_z peak is slightly lower than the peak 1 minute earlier, which may suggest that the "re-reconnection" still plays a role to erase the northward magnetic flux in the dipolarization region but is not able to annihilate the whole structure.

[26] As the BBF and DF approach the inner magnetosphere, the BBF front starts to slow down and is diverted, which can be clearly seen on Figure 13e at 0751 UT. The diversion and reflection of the earthward BBF start to produce tailward flows on both sides of the earthward flow channel. The tailward reflected flows are enhanced on the east side of the earthward BBF at 0753 UT as shown in Figure 14a. It is interesting that the dipolarization region appears to separate into two parts and that the tailward part starts to move antisunward with the reflected tailward flow at 0754 UT (Figure 14b). This tailward motion of a separate dipolarization region persists until the following earthward flows brings it back (Figures 14c–14f). The oscillation of tail flows and dipolarization regions is similar to the recent THEMIS observation of the multiple overshoot and rebound of a BBF [*Panov et al.*, 2010a, 2010b]. The overshoot signature of the BBF can be found in the simulation signaled by the concave indentation on the inner dipole dominating region shown on Figure 14a. This indentation eventually recovers when the dipolarization region starts to expand or move tailward, suggesting the restoration of the force balance.

[27] Besides reflection and diversion, other interactions of the BBF and the DF in the front of it with the background plasma can be seen in our simulation. In Figure 13b, a region with the Bz enhancement penetrates into the background plasma along with the earthward flows produced by the inner reconnection at X = −13 R_E and Y = 5 R_E. The penetrated strong field region grows as more and more earthward flows move in along the previous path and forms an Ω-shaped region of enhanced field region inside of 9 R_E in the premidnight sector of the near-Earth tail. This structure with the enhanced magnetic field strength appears to have lower plasma pressure (not shown), which is similar to

the low-entropy magnetic flux tubes in the magnetotail that are often referred to as "plasma bubbles" [*Birn et al.*, 2004].

[28] Another interesting result from this simulation is that the dipolarization front surface itself appears to be unstable to the Rayleigh-Taylor or interchange instability. At 0751 UT (Figure 13e), we can find that the wavy surface appears on the dipolarization front as it approaches the inner magnetosphere. The wavelength of this wavy structure (from peak to peak) is about 1 R_E or less, and this short fingerlike structures persists, e.g., the quasiperiodic structure between the DF and the inner dipole field at 0752 UT (Figure 13f) until it merges with the background plasma. This filamentation of the incoming DF has also been shown by *Pritchett and Coroniti* [2010]. But the possible Rayleigh-Taylor instability never fully develops because the DF merges with the dipolar inner magnetosphere, which removes the entropy gradient necessary for the instability. It is outside the scope of this study to further investigate these structures, which will be pursued in our future work.

5. Conclusions and Discussion

[29] In this study, we use the OpenGGCM model to simulate the THEMIS substorm on 27 February 2009. Overall, the OpenGGCM reproduces well the key features of the observed dynamical changes in the magnetosphere and ionosphere. The auroral breakup, poleward expansion, and westward traveling in the field of view of the ground station Fort Smith (FSMI) is reproduced in the simulation with a similar onset time, ~0751 UT. This auroral breakup is found in the simulation to be associated with a strong earthward BBF generated from an X-line at around 25 R_E. The strong earthward BBF produces a strong flow shearing on the edges of the flow channel, especially on the west side edge, where the preexisting tailward flows from a earlier and inner reconnection enhances the flow shearing and thus generates strong vorticity in the flow. It is found that the auroral breakup on FSMI maps into the west side edge of the earthward BBF channel and the brightening region moves westward as the BBF channel shifts duskward. This simulation result is consistent with earlier studies on the relation of tail flow bursts and auroral activities. For example, using Geotail and Polar observations, *Nakamura et al.* [2001] found that some auroral activities, especially auroral streamers, pseudo-breakups, and small substorm breakups, were directly connected with the earthward BBFs and map into the west edge of these BBFs.

[30] A dipolarization front forms in front of this BBF during its motion toward the Earth. The structure of the dipolarization front that has a decreased Bz signature in front of the DF is also reproduced, and the diamagnetic effect inferred by *Runov et al.* [2009] in this event has been seen in the simulation. This structure is found in this global MHD simulation to be generated by the interaction of preexisting tailward flows from a closer reconnection to the Earth with the strong earthward BBF from the midtail reconnection. This result is consistent with the explanation suggesting that the bipolar change of the Bz component at the dipolarization front comes from the multiple X-lines in the tail [*Ohtani et al.*, 2004; *Slavin et al.*, 2003]. The thickness of this structure in our study is limited by the spatial resolution of our simulations and in the steepest

dipolarization front the thickness is about 0.6 R_E, which is about two or three grid cells in the simulation. It is important to note that in our global simulations, the multiple X-lines are not required to occur in the same local time to produce this DF structure. In fact, in the simulation we find that two reconnection sites are located at the premidnight and postmidnight sectors, respectively, and the magnetic field produced by a reconnection site closer to the Earth (at ~13 R_E) resulted in the observed DF structures. Also, from the interaction between these tailward flows with another earthward BBF, we can find that once the inner reconnection is strong, the earthward flowing BBF may be stopped on its way to the inner magnetosphere if it propagates along the same local time as that of the inner reconnection and even can be dissipated during the "re-reconnection" with the southward magnetic flux from the inner reconnection. However, it is also worth noting that our single-event study of the DF structure does not rule out the Nightside-FTE (NFTE) scenario proposed by *Sergeev et al.* [1992], since our grid setting may be too rough to capture the signatures of NFTE.

[31] This simulation also produces a picture of the interaction between the intruding BBF and the background plasma. Once the BBF encounters the high-pressure region of the dipole field, it slows and is diverted toward both sides of the original channel, which produces enhanced tailward flows and forms flow vortices. The reflected tailward flows result in a rebound signature of plasma flows, which is similar to the recent observations by *Panov et al.* [2010a, 2010b]. The overshoot of the intruding BBF can also be seen in Figure 14 by the concave indentation of the high-pressure region where the BBF impacts. In our simulations, the tailward motion of a dipolarization region is stopped by the following intruding BBF, which produces an oscillation-like motion of the dipolarization region.

[32] Some other results from the simulations are also interesting but only briefly mentioned. For example, we find that the inner magnetic reconnection produces bubble-like structures that penetrate deeply into the inner magnetosphere, although the flows that bring the depleted flux tubes are not as strong as those from the midtail reconnection. The penetrating flux tubes or the enhanced dipolarization region grows and forms an Ω-shaped region inside of 10 R_E. Also, we find that some fluid instabilities such as Rayleigh-Taylor or interchange instability may be triggered as the BBF approaches the inner magnetosphere and interacts with the background plasma. The wavelength of the short fingerlike structures on the surface of the DF is found to be about 1 R_E. These dynamical features brought by the intruding BBF with the background plasma and their roles in near-Earth tail dynamics shall be further identified and studied in our future work.

References

Angelopoulos, V., W. Baumjohann, C. F. Kennel, F. V. Coroniti, M. G. Kivelson, R. Pellat, R. J. Walker, H. Luhr, and G. Paschmann (1992), Bursty bulk flows in the inner central plasma sheet, *J. Geophys. Res.*, *97*(A4), 4027–4039, doi:10.1029/91JA02701.

Angelopoulos, V., C. F. Kennel, F. V. Coroniti, R. Pellat, M. G. Kivelson, R. J. Walker, C. T. Russell, W. Baumjohann, W. C. Feldman, and J. T. Gosling (1994), Statistical characteristics of bursty bulk flow events, *J. Geophys. Res.*, *99*(A11), 21,257–21,280, doi:10.1029/94JA01263.

Angelopoulos, V., et al. (2008), First results from THEMIS mission, *Space Sci. Rev.*, *141*, 453–476, doi:10.1007/s11214-008-9378-4.

Baumjohann, W., G. Paschmann, and H. Luhr (1990), Characteristics of high-speed ion flows in the plasma sheet, *J. Geophys. Res.*, *95*(A4), 3801–3809, doi:10.1029/JA095iA04p03801.

Baumjohann, W., G. Paschmann, T. Nagai, and H. Luhr (1991), Super-posed epoch analysis of the substorm plasma sheet, *J. Geophys. Res.*, *96*(A7), 11,605–11,608, doi:10.1029/91JA00775.

Baumjohann, W., M. Hesse, S. Kokubun, T. Mukai, T. Nagai, and A. A. Petrukovich (1999), Substorm dipolarization and recovery, *J. Geophys. Res.*, *104*(A11), 24,995–25,000, doi:10.1029/1999JA900282.

Birn, J., and M. Hesse (1991), The substorm current wedge and field-aligned currents in MHD simulations of magnetotail reconnection, *J. Geophys. Res.*, *96*(A2), 1611–1618, doi:10.1029/90JA01762.

Birn, J., and M. Hesse (1996), Details of current disruption and diversion in simulations of magnetotail dynamics, *J. Geophys. Res.*, *101*(A7), 15,345–15,358, doi:10.1029/96JA00887.

Birn, J., M. Hesse, G. Haerendel, W. Baumjohann, and K. Shiokawa (1999), Flow braking and the substorm current wedge, *J. Geophys. Res.*, *104*(A9), 19,895–19,903, doi:10.1029/1999JA900173.

Birn, J., J. Raeder, Y. L. Wang, R. A. Wolf, and M. Hesse (2004), On the propagation of bubbles in the geomagnetic tail, *Ann. Geophys.*, *22*(5), 1773–1786.

Fuller-Rowell, T. J., D. Rees, S. Quegan, R. J. Moffett, M. V. Codrescu, and G. H. Millward (1996), A coupled thermosphere-ionosphere model (CTIM), in *STEP Report*, edited by R. W. Schunk, SCOSTEP, Boulder, Colo.

Hesse, M., and J. Birn (1991), On dipolarization and its relation to the sub-storm current wedge, *J. Geophys. Res.*, *96*(A11), 19,417–19,426, doi:10.1029/91JA01953.

Hsu, T.-S., and R. L. McPherron (2007), A statistical study of the relation of Pi2 and plasma flows in the tail, *J. Geophys. Res.*, *112*, A05209, doi:10.1029/2006JA011782.

Ieda, A., D. H. Fairfield, T. Mukai, Y. Saito, S. Kokubun, K. Liou, C. I. Meng, G. K. Parks, and M. J. Brittnacher (2001), Plasmoid ejection and auroral brightenings, *J. Geophys. Res.*, *106*(A3), 3845–3857, doi:10.1029/1999JA000451.

Keiling, A., et al. (2009), Substorm current wedge driven by plasma flow vortices: THEMIS observations, *J. Geophys. Res.*, *114*, A00C22, doi:10.1029/2009JA014114.

Kennel, C. F., and H. E. Petschek (1966), Limit on stably trapped particle fluxes, *J. Geophys. Res.*, *71*(1), 1–28, doi:10.1029/JZ071i001p00001.

Lyons, L. R., D. S. Evans, and R. Lundin (1979), An observed relation between magnetic-field aligned electric-fields and downward electron-energy fluxes in the vicinity of auroral forms, *J. Geophys. Res.*, *84*(A2), 457–461, doi:10.1029/JA084iA02p00457.

Lyons, L. R., T. Nagai, G. T. Blanchard, J. C. Samson, T. Yamamoto, T. Mukai, A. Nishida, and S. Kokubun (1999), Association between Geotail plasma flows and auroral poleward boundary intensifications observed by CANOPUS photometers, *J. Geophys. Res.*, *104*(A3), 4485–4500, doi:10.1029/1998JA900140.

Mende, S. B., S. E. Harris, H. U. Frey, V. Angelopoulos, C. T. Russell, E. Donovan, B. Jackel, M. Greffen, and L. M. Peticolas (2008), The THEMIS array of ground-based observatories for the study of auroral substorms, *Space Sci. Rev.*, *141*(1–4), 357–387, doi:10.1007/s11214-008-9380-x.

Miyashita, Y., S. Machida, K. Liou, T. Mukai, Y. Saito, H. Hayakawa, C. I. Meng, and G. K. Parks (2003), Evolution of the magnetotail associated with substorm auroral breakups, *J. Geophys. Res.*, *108*(A9), 1353, doi:10.1029/2003JA009939.

Nagai, T., M. Fujimoto, Y. Saito, S. Machida, T. Terasawa, R. Nakamura, T. Yamamoto, T. Mukai, A. Nishida, and S. Kokubun (1998), Structure and dynamics of magnetic reconnection for substorm onsets with Geotail observations, *J. Geophys. Res.*, *103*(A3), 4419–4440, doi:10.1029/97JA02190.

Nakamura, R., W. Baumjohann, R. Schodel, M. Brittnacher, V. A. Sergeev, M. Kubyshkina, T. Mukai, and K. Liou (2001), Earthward flow bursts, auroral streamers, and small expansions, *J. Geophys. Res.*, *106*(A6), 10,791–10,802, doi:10.1029/2000JA000306.

Nakamura, R., et al. (2002), Motion of the dipolarization front during a flow burst event observed by Cluster, *Geophys. Res. Lett.*, *29*(20), 1942, doi:10.1029/2002GL015763.

Nakamura, R., et al. (2005), Cluster and double star observations of dipo-larization, *Ann. Geophys.*, *23*(8), 2915–2920.

Nakamura, R., A. Retino, W. Baumjohann, M. Volwerk, N. Erkaev, B. Klecker, E. A. Lucek, I. Dandouras, M. Andre, and Y. Khotyaintsev (2009), Evolution of dipolarization in the near-Earth current sheet induced by earthward rapid flux transport, *Ann. Geophys.*, *27*(4), 1743–1754.

Ohtani, S., R. Yamaguchi, M. Nose, H. Kawano, M. Engebretson, and K. Yumoto (2002a), Quiet time magnetotail dynamics and their impli-cations for the substorm trigger, *J. Geophys. Res.*, *107*(A2), 1030, doi:10.1029/2001JA000116.

Ohtani, S., R. Yamguchi, H. Kawano, F. Creutzberg, J. B. Sigwarth, L. A. Frank, and T. Mukai (2002b), Does the braking of the fast plasma flow trigger a substorm?: A study of the August 14, 1996, event, *Geophys. Res. Lett.*, *29*(15), 1721, doi:10.1029/2001GL013785.

Ohtani, S., M. A. Shay, and T. Mukai (2004), Temporal structure of the fast convective flow in the plasma sheet: Comparison between observations and two-fluid simulations, *J. Geophys. Res.*, *109*, A03210, doi:10.1029/2003JA010002.

Panov, E. V., et al. (2010a), Multiple overshoot and rebound of a bursty bulk flow, *Geophys. Res. Lett.*, *37*, L08103, doi:10.1029/2009GL041971.

Panov, E. V., et al. (2010b), Plasma sheet thickness during a bursty bulk flow reversal, *J. Geophys. Res.*, *115*, A05213, doi:10.1029/2009JA014743.

Pritchett, P. L., and F. V. Coroniti (2010), A kinetic ballooning/interchange instability in the magnetotail, *J. Geophys. Res.*, *115*, A06301, doi:10.1029/2009JA014752.

Raeder, J., J. Berchem, and M. Ashour-Abdalla (1996), The importance of small scale processes in global MHD simulations: Some numerical ex-periments, in *The Physics of Space Plasmas*, edited by T. Chang and J. R. Jasperse, p. 403, MIT Cent. for Theoret. Geo/Cosmo Plasma Phys., Cambridge, Mass.

Raeder, J., J. Berchem, and M. Ashour-Abdalla (1998), The geospace envi-ronment modeling grand challenge: Results from a global geospace cir-culation model, *J. Geophys. Res.*, *103*(A7), 14,787–14,797, doi:10.1029/98JA00014.

Raeder, J., Y. L. Wang, and T. Fuller-Rowell (2001a), Geomagnetic storm simulation with a coupled magnetosphere-ionosphere-thermosphere model, in *Space Weather*, *Geophys. Monogr. Ser.*, vol. 125, edited by P. Song, G. L. Siscoe, and H. Singer, p. 377, AGU, Washington, D. C.

Raeder, J., Y. L. Wang, T. J. Fuller-Rowell, and H. J. Singer (2001b), Global simulation of magnetospheric space weather effects of the Bastille Day storm, *Sol. Phys.*, *204*(1–2), 325–338.

Raeder, J., R. L. McPherron, L. A. Frank, S. Kokubun, G. Lu, T. Mukai, W. R. Paterson, J. B. Sigwarth, H. J. Singer, and J. A. Slavin (2001c), Global simulation of the geospace environment modeling substorm chal-lenge event, *J. Geophys. Res.*, *106*(A1), 381–395, doi:10.1029/2000JA000605.

Raeder, J., D. Larson, W. H. Li, E. L. Kepko, and T. Fuller-Rowell (2008), OpenGGCM Simulations for the THEMIS mission, *Space Sci. Rev.*, *141*(1–4), 535–555, doi:10.1007/s11214-008-9421-5.

Robinson, R. M., R. R. Vondrak, K. Miller, T. Dabbs, and D. Hardy (1987), On calculating ionospheric conductances from the flux and energy of precipitating electrons, *J. Geophys. Res.*, *92*(A3), 2565–2569, doi:10.1029/JA092iA03p02565.

Runov, A., V. Angelopoulos, M. I. Sitnov, V. A. Sergeev, J. Bonnell, J. P. McFadden, D. Larson, K. H. Glassmeier, and U. Auster (2009), THEMIS observations of an earthward-propagating dipolarization front, *Geophys. Res. Lett.*, *36*, L14106, doi:10.1029/2009GL038980.

Russell, C. T., P. J. Chi, D. J. Dearborn, Y. S. Ge, B. Kuo-Tiong, J. D. Means, D. R. Pierce, K. M. Rowe, and R. C. Snare (2008), THEMIS ground-based magnetometers, *Space Sci. Rev.*, *141*(1–4), 389–412, doi:10.1007/s11214-008-9337-0.

Scholer, M., and A. Otto (1991), Magnetotail reconnection: Current diver-sion and field-aligned currents, *Geophys. Res. Lett.*, *18*(4), 733–736, doi:10.1029/91GL00361.

Sergeev, V. A., R. C. Elphic, F. S. Mozer, A. Saintmarc, and J. A. Sauvaud (1992), A 2-satellite study of nightside flux-transfer events in the plasma sheet, *Planet. Space Sci.*, *40*(11), 1551–1572.

Sergeev, V. A., V. Angelopoulos, D. G. Mitchell, and C. T. Russell (1995), In situ observations of magnetotail reconnection prior to the onset of a small substorm, *J. Geophys. Res.*, *100*(A10), 19,121–19,133, doi:10.1029/95JA01471.

Shiokawa, K., W. Baumjohann, and G. Haerendel (1997), Braking of high-speed flows in the near-Earth tail, *Geophys. Res. Lett.*, *24*(10), 1179–1182, doi:10.1029/97GL01062.

Shiokawa, K., et al. (1998), High-speed ion flow, substorm current wedge, and multiple Pi2 pulsations, *J. Geophys. Res.*, *103*(A3), 4491–4507, doi:10.1029/97JA01680.

Sitnov, M. I., M. Swisdak, and A. V. Divin (2009), Dipolarization fronts as a signature of transient reconnection in the magnetotail, *J. Geophys. Res.*, *114*, A04202, doi:10.1029/2008JA013980.

Slavin, J. A., R. P. Lepping, J. Gjerloev, D. H. Fairfield, M. Hesse, C. J. Owen, M. B. Moldwin, T. Nagai, A. Ieda, and T. Mukai (2003), Geotail observations of magnetic flux ropes in the plasma sheet, *J. Geophys. Res.*, *108*(A1), 1015, doi:10.1029/2002JA009557.

Tang, C. L., V. Angelopoulos, A. Runov, C. T. Russell, H. Frey, K. H. Glassmeier, K. H. Fornacon, and Z. Y. Li (2010), Precursor activation and substorm expansion associated with observations of a dipolarization front by Thermal Emission Imaging System (THEMIS), *J. Geophys. Res.*, *115*, A07215, doi:10.1029/2009JA014879.

Weimer, D. R., D. A. Gurnett, C. K. Goertz, J. D. Menietti, J. L. Burch, and M. Sugiura (1987), The current-voltage relationship in auroral current sheets, *J. Geophys. Res.*, *92*(A1), 187–194, doi:10.1029/JA092iA01p00187.

V. Angelopoulos and A. Runov, Institute of Geophysics and Planetary Physics, University of California, 3845 Slichter Hall, Los Angeles, CA 90095, USA.

Y. S. Ge, M. L. Gilson, and J. Raeder, Space Science Center, University of New Hampshire, Morse Hall, 8 College Rd., Durham, NH 03824, USA. (yasong.ge@gmail.com)